Small-amplitude perturbations in the three-dimensional cylindrical Richtmyer–Meshkov instability

M. Lombardini[a] and D. I. Pullin
Graduate Aeronautical Laboratories, California Institute of Technology, Pasadena, California 91125, USA

(Received 13 May 2009; accepted 8 September 2009; published online 6 November 2009)

We first study the linear stability of an interface between two fluids following the passage of an imploding or exploding shock wave. Assuming incompressible flow between the refracted waves following shock impact, we derive an expression for the asymptotic growth rate for a three-dimensional combination of azimuthal and axial perturbations as a function of the Atwood ratio, the axial and azimuthal wave numbers, the initial radial position and perturbation amplitude of the interface, and the interface velocity gain due to the shock interaction. From the linearized theory, a unified expression for the impulsive asymptotic growth rate in plane, cylindrical, and spherical geometries is obtained which clearly delineates the effects of perturbation growth due to both geometry and baroclinic vorticity deposition. Several different limit cases are investigated, allowing recovery of Mikaelian's purely azimuthal theory and Richtmyer's plane model. We discuss the existence of three-dimensional perturbations with zero growth, typical of curvilinear geometries, as first observed by Mikaelian. The effect of shock proximity on the interface growth rate is studied in the case of a reflected shock. Analytical predictions of the effect of the incident shock strength and the perturbation wave numbers are then compared with results obtained from highly resolved numerical simulations of cylindrical imploding Richtmyer–Meshkov instability for ideal gases. A parallel is made with the instability growth in spherical and plane geometry. In particular, we propose a representation of the perturbation growth by considering the volume of the perturbed layer. This volume is found to grow faster in the plane case than in the imploding cylindrical geometry, among other results. © *2009 American Institute of Physics*. [doi:10.1063/1.3258668]

I. INTRODUCTION

The Richtmyer–Meshkov instability (RMI) refers to the evolution of perturbations at an interface separating two fluids of different densities impacted by a shock. In plane geometry, small amplitude or linear perturbation growth rates reach an asymptotic level first predicted by Richtmyer[1] and confirmed qualitatively by the experiments of Meshkov.[2]

Examples of the occurrence of RMI in converging geometries, in particular, the cylindrical geometry, are present in experiments aiming to achieve inertial confinement fusion[3] (ICF) or in natural phenomena such as supernova collapse.[4] Although experiments on fluid mixing in cylindrical and spherical geometries have been conducted to elucidate shock convergence effects,[5–7] open questions remain; see Sec. V in Ref. 8 for a detailed discussion. In parallel, Dimotakis and Samtaney[9] theoretically designed a gas lensing technique that can smoothly focus a plane shock into a segment of a circular cylinder in a two-dimensional wedge geometry, a first step toward canonical experiments of the converging RMI. Two-dimensional simulations of the instability in polar geometries for imploding and exploding shocks using a front-tracking method have also been performed.[10]

The research cited previously concerns mainly the nonlinear and/or multimode regime of the RMI initialized with large perturbation amplitudes, as well as the reshock process and the subsequent turbulent mixing. Analytical work has also been reported on the effects of convergence on the linear or small amplitude regime of RMI occurring in spherical[11] and cylindrical purely azimuthal[8] stratified shells. For simplicity, compressible effects often observed in the RMI of gases (such as shock refraction, shock proximity effects, etc. as discussed, for example, in Refs. 12 and 13) were omitted by considering incompressible fluids. These effects are naturally non-negligible in geometrically convergent configurations involving gases.

In curved geometry, the perturbation growth at a shocked interface is not only due to the initial impulsive deposition of vorticity, but also to the interface radial motion itself. This is usually the case for ICF applications where both accelerating force and ablative front contribute to the instability. The distinction between both geometrical effects, combined with the compressibility effects, is usually difficult to assess. Aiming for this direction, a recent interesting contribution[14] studied the case of three-dimensional cylindrical single-mode perturbations at a continuously accelerated/decelerated interface, therefore focusing on the continuous counterpart of the RMI, also known as the Rayleigh–Taylor instability[15] (RTI). Modes were searched with an exponential growth in time. Unfortunately, this method is not suitable for the RMI whose small-amplitude growth rate is known to be approximately linear in time in the plane case.

Presently we study several features of the three-dimensional cylindrical RMI in the linear regime using both

[a]Electronic mail: manuel@caltech.edu.

simple analysis and numerical Euler-based simulations. The analysis of Sec. II first extends to three-dimensional azimuthal and axial perturbations, the results of Mikaelian (in the case of one shell). The effect of proximity of the transmitted and reflected shocks produced by a light-to-heavy initial shock refraction is also modeled following the methodology described in Ref. 13. Section III compares the results from the linearized analysis to numerical simulations of the converging RMI for ideal gases under various initial conditions. The effects of azimuthal and axial wave numbers for different incident shock strengths and a comparison to the plane and converging spherical geometries are exposed.

II. INCOMPRESSIBLE LINEAR THEORY FOR THREE-DIMENSIONAL CYLINDRICAL PERTURBATIONS

A. General evolution equations

The interaction of a shock with a perturbed density interface is an atypical hydrodynamics stability problem. The shock refraction process produces distorted transmitted and reflected waves in the vicinity of the interface. The related perturbed pressure field induces perturbations in the tangential component of the velocity field to the interface, producing circulation that can be directly related to the initial baroclinic vorticity deposited at the interface. In what follows, $t=0$ refers to the time right when the shock impacts the interface in the zeroth order or unperturbed flow. We denote by the subscript $j=1$ the region on the outer side of the interface, and by $j=2$, the region on the inner side of the interface, including the axis.

The stability of density interfaces in converging geometries was studied by Plesset[16] in the particular case of spherical bubbles ($\rho_2 \ll \rho_1$). For imploding flows, a sinklike motion with axis $r=0$ was used to produce flow/interface contraction while maintaining constant density. Following Plesset and Mikaelian,[8] we model our base flow as an incompressible impulse sink of strength to be determined of the form $m(t)=\mu(t)H(t)$ with velocity potential

$$\Phi(r,t) = m(t)\ln\left(\frac{r}{R(t)}\right), \tag{1}$$

$R(t)$ being the base radial position of the interface and $H(t)$ the Heaviside function at time t. For an imploding flow, $\mu(t)<0$ for $t\geq 0$. At this point, $\mu(t)$ and $R(t)$ remain to be specified. The base velocity field is given by

$$\boldsymbol{U}(r,t) = \frac{m(t)}{r}\boldsymbol{e}_r. \tag{2}$$

We consider three-dimensional azimuthal and axial infinitesimal perturbations about the time-dependent state $R(t)$ of the form

$$\begin{aligned} \phi_j'(r,\theta,z,t) &= f_j(r)g_j(t)e^{i(n\theta+kz)}, \\ \zeta(\theta,z,t) &= R(t) + h(t)e^{i(n\theta+kz)}. \end{aligned} \tag{3}$$

The perturbed potential $\phi_j'(r,\theta,z,t)$ for the gas j ($j=1,2$) is assumed to be separable in r and t; $\zeta(\theta,z,t)$ is the perturbed position of the interface, where the integers n and k represent, respectively, the azimuthal and axial wave numbers and are assumed not to be functions of time. The present assumptions of incompressible and irrotational flow on each side of the interface are discussed subsequently.

When the interface is strictly cylindrical, a kinematic condition that the radial velocity is continuous at the interface and equal to an interfacial particle velocity gives that

$$\dot{R} = \left(\frac{\partial\Phi}{\partial r}\right)_{r=R}, \tag{4}$$

which leads to

$$\mu = R\dot{R}. \tag{5}$$

Full knowledge of the base flow therefore requires specification of the implosion/explosion history $R(t)$, at least for times such that the perturbation growth remains linear. R is at least piecewise continuous at $t=0$ with $R_0 \equiv R(t=0)$. The interface speed $\dot{R}$ and the potential strength μ may be discontinuous at $t=0$. The jump in $\dot{R}$ around $t=0$ simply represents the impulsive change in the interface velocity ΔW modeling the shock interaction. For an implosion (respectively explosion) the jump in radial velocity is $-\Delta W<0$ (respectively $\Delta W>0$). ΔW and other quantities, such as the densities of the two postshock regions, can be computed by solving the locally plane interaction of the incident shock with the unperturbed interface. Requiring that the base pressure field be continuous at the interface and using Bernoulli's theorem shows that

$$\begin{aligned} &\rho_1\left[\frac{\partial\Phi}{\partial t} + \frac{1}{2}\left(\frac{\partial\Phi}{\partial r}\right)^2 - C_1(t)\right]_{r=R} \\ &\quad = \rho_2\left[\frac{\partial\Phi}{\partial t} + \frac{1}{2}\left(\frac{\partial\Phi}{\partial r}\right)^2 - C_2(t)\right]_{r=R}. \end{aligned} \tag{6}$$

Consider now the distorted interface. The kinematic condition $D\zeta/Dt=(\boldsymbol{u}\cdot\boldsymbol{n})_{r=\zeta}$, where $\boldsymbol{u}$ is the velocity field and $\boldsymbol{n}$ is the local normal to the interface, can be linearized and simplified as follows using the base kinematic condition (4):

$$R\dot{h} + \dot{R}Hh = g_j R f_j'(R), \quad \text{for } j=1,2. \tag{7}$$

Similarly, a dynamic condition is obtained by linearizing the continuity of pressure at the perturbed interface and using Eq. (6) to give

$$\begin{aligned} &R\dot{R}H\dot{h} + [(\dot{R}^2 + R\ddot{R})H + R\dot{R}\delta_D]h \\ &\quad = \frac{R}{2A}[(1-A)f_1(R)\dot{g}_1 - (1+A)f_2(R)\dot{g}_2], \end{aligned} \tag{8}$$

where $\delta_D(t)$ is the Dirac delta function and $A=(\rho_2-\rho_1)/(\rho_2+\rho_1)$ represents the Atwood number based on the densities on each side of the interface. In the early regime of the perturbation growth, $A(t)$ approaches a piecewise constant function of t. For simplicity, in what follows A will be identified with the postshock Atwood number A^+ given by the postshock densities.

B. Asymptotic growth rate

In the impulsive approach of Richtmyer, the passage of the shock impacting a perturbed density interface is modeled by an initial deposition of baroclinic vorticity on the interface by a delta-function acceleration, assuming that waves resulting from the initial shock refraction have already traveled far from the interface, leaving behind a quasi-incompressible flow. In this incompressible-flow approximation the vorticity is essentially localized at the interface and evolves solely from its initial distribution, while the fluid motion on each side of the interface is irrotational. The range of validity of this incompressible and irrotational assumption can in fact be related directly to the proximity of the refracted waves to the interface in the real compressible flow. Besides the baroclinic deposition of vorticity during the initial shock passage and the vortex-accelerated secondary baroclinic vorticity deposition, there are two other contributions to the vorticity field surrounding the interface: bulk vorticity deposition by relaxation of deformed refracted wave fronts and baroclinic deposition on the interface by reverberation of acoustic waves emitted by the deformed refracted waves. Both assumptions are therefore valid in the weak incident shock wave limit where the refracted waves recede away from the interface faster, relative to the time scale for interface growth, than for strong incident shocks.

Similarly, ignoring for now the refracted waves and assuming that no reshock has yet occurred following shock reflection off the axis, an imploding shock interaction results in two postshock regions on each side of the interface: $\zeta<r<\infty$ for region $j=1$ and $0<r<\zeta$ for region $j=2$. The functions $f_j(r)$, $j=1,2$ are fully determined by solving the Laplace equation for the perturbed potential $\Delta\phi_j'=0$ on each side of the interface. The $f_j(r)$ are generally a linear combination of the modified Bessel functions of the first and second kinds, $I_n(kr)$ and $K_n(kr)$. For the fluid $j=1$ (region $r>\zeta$), the boundary condition $\nabla\phi_1'\to 0$ as $r\to+\infty$ is prescribed. For the fluid $j=2$ (region $0<r<\zeta$), ϕ_2' should remain nonsingular as $r\to 0$. We then obtain

$$f_1(r)=\begin{cases} K_n(kr); & k>0 \\ \left(\dfrac{R_0}{r}\right)^n; & k=0 \end{cases}, \quad f_2(r)=\begin{cases} I_n(kr); & k>0 \\ \left(\dfrac{r}{R_0}\right)^n; & k=0. \end{cases} \tag{9}$$

Naturally h is continuous at $t=0$, and $h(0)\equiv\lim_{t\to 0} h(t)$, but for an impulsively accelerated flow, the g_j as well as $\dot{h}$ are discontinuous around $t=0$. Integrating the linearized dynamic condition (8) between $t=0^-$ and 0^+ and using Eq. (7), the growth rate of the three-dimensional cylindrical perturbation, as well as the perturbed potential functions g_j, is found at $t=0^+$,

$$\dot{h}(0^+)=\frac{h(0)}{R_0}\Delta W[1+\kappa A F(n,\kappa,A)], \tag{10a}$$

$$g_1(0^+)=h(0)\Delta W A\frac{F(n,\kappa,A)}{K_n'(\kappa)}, \tag{10b}$$

$$g_2(0^+)=h(0)\Delta W A\frac{F(n,\kappa,A)}{I_n'(\kappa)}, \tag{10c}$$

where $F(n,\kappa,A)$ is given by

$$F(n,\kappa,A)=1\Big/\left(\frac{1+A}{2}\frac{I_n(\kappa)}{I_n'(\kappa)}-\frac{1-A}{2}\frac{K_n(\kappa)}{K_n'(\kappa)}\right), \tag{11}$$

and where we defined a dimensionless axial wave number $\kappa=kR_0$. The result obtained for the growth rate assumes that transmitted and reflected waves are at large distances from the interface at $t=0$. In that sense, the time $t=0^+$ after the passage of the incident shock could refer to an asymptotic state, and Eq. (10a) would lead to the asymptotic growth rate in the sense of Richtmyer's modeling, whose complete expression is

$$\dot{h}(0^+)=\frac{h(0)}{R_0}\Delta W \times\left[1+kR_0A\Big/\left(\frac{1+A}{2}\frac{I_n(kR_0)}{I_n'(kR_0)}-\frac{1-A}{2}\frac{K_n(kR_0)}{K_n'(kR_0)}\right)\right]. \tag{12}$$

Note that as the linear growth rate in the plane RMI, the asymptotic growth rate is proportional to the amplitude $h(0)$ at $t=0$, as well as ΔW, in other terms $-\dot{R}(0^+)$ for an imploding flow. The interface postshock acceleration $\ddot{R}(0^+)$ does not appear in the initial growth rate as a result of linearizing the problem around $t=0$.

In order to compare the asymptotic growth rate obtained in cylindrical geometry with its plane counterpart for a given A, we plot in Fig. 1 the difference between the growth rates given by Eq. (10a) and Richtmyer for a two-dimensional plane perturbation with equivalent orthogonal wave numbers k and n/R_0. The following paragraph supports the results of Fig. 1.

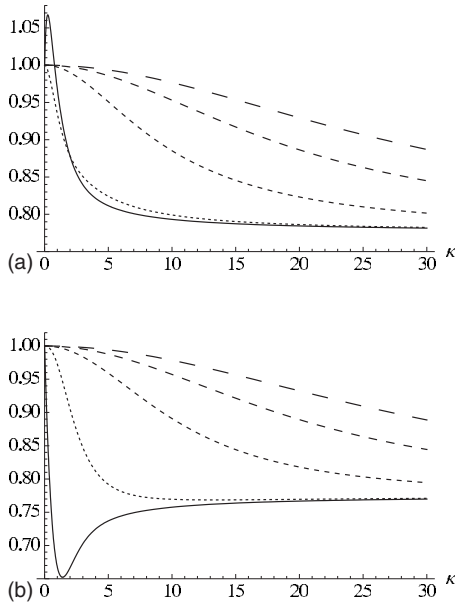

FIG. 1. Difference between the (dimensionless) cylindrical growth rate and its plane counterpart $[1+\kappa AF(n,\kappa,A)]-\sqrt{n^2+\kappa^2}A$ vs $\kappa \equiv kR_0$ for $n=0$ (solid line), $n=2$ (dotted line), $n=10$ (small dashed line), $n=20$ (dashed line), and $n=40$ (long dashed line) for two different Atwood ratios: (a) $A=-0.61$ and (b) $A=0.61$.

1. Limit cases

We enumerate several limit cases in A,

$$\dot{h}(0^+) \sim \frac{h(0)}{R_0}\Delta W \quad \text{if } A \to 0, \quad \text{i.e., } \rho_1 \sim \rho_2, \tag{13a}$$

$$\dot{h}(0^+) \sim \frac{h(0)}{R_0}\Delta W\left(1+\kappa\frac{I_n'(\kappa)}{I_n(\kappa)}\right) \quad \text{if } A \to 1, \quad \text{i.e., } \rho_1 \ll \rho_2, \tag{13b}$$

$$\dot{h}(0^+) \sim \frac{h(0)}{R_0}\Delta W\left(1+\kappa\frac{K_n'(\kappa)}{K_n(\kappa)}\right) \quad \text{if } A \to -1, \quad \text{i.e., } \rho_1 \gg \rho_2. \tag{13c}$$

As $A \to 0$ the growth is purely kinematic, an effect specific to curved geometry. To verify this, consider a fluid element at radius $R(t)+h(t)$, whose base velocity is $\mu(t)/[R(t)+h(t)]$, and a fluid element at radius $R(t)$ with velocity $\mu(t)/R(t)$. Growth naturally appears due to this difference in velocities and produces a growth rate equal to $h(0)\Delta W/R_0$.

Some other interesting limit cases are obtained when varying κ and n,

$$\dot{h}(0^+) \sim \frac{h(0)}{R_0}\Delta W(1+nA) \quad \text{if } \kappa \ll n \quad \text{and} \quad n \geq 1, \tag{14a}$$

$$\dot{h}(0^+) \sim \frac{h(0)}{R_0}\Delta W\left(1+n\frac{2A}{1+A}\right) \quad \text{if } \kappa \ll 1 \quad \text{and} \quad n \ll 1, \tag{14b}$$

$$\dot{h}(0^+) \sim \frac{h(0)}{R_0}\Delta W(1+\kappa A) \quad \text{if } \kappa \gg n \quad \text{and} \quad \kappa \gg 1. \tag{14c}$$

Equation (14a) corresponds to purely azimuthal perturbations as obtained in Ref. 8, where the wavelengths verify $\lambda_\theta \ll \lambda_z$ (strictly polar flow). The limit behavior presented in Eq. (14c) corresponds to purely axial perturbations. In this case, the effects of the convergence are only seen through the kinematic growth term. The linear growth, excluding the kinematic growth component, is $kh(0)A\Delta W$ with $\Delta W=-\dot{R}(0^+)$, similar to Richtmyer's plane linear growth of perturbations along the z-direction.

Motivated by the latter observations, we can formulate the asymptotic growth rate of a single-mode perturbation at an impulsively accelerated interface in various geometries. The plane case (space index $s=1$) has been initially derived by Richtmyer,[1] while we derived here the cylindrical case ($s=2$) as an extension of Bell and Mikaelian's purely cylindrical azimuthal perturbation models.[8,17] The perturbation evolution in spherical geometry ($s=3$) is given by Eq. (14) in Ref. 16 after expanding the perturbations in spherical harmonics $Y_{m,n}$ and assuming no surface tension on the interface. Integrating this equation around $t=0$, an expression for the asymptotic growth rate in spherical geometry can be straightforwardly obtained as a function of A and the mode m. We finally obtained for $s=1$, 2, and 3,

$$\dot{h}(0^+) = \frac{h(0)}{R_0}\Delta W(s-1+F_s), \tag{15a}$$

$$F_1 = \kappa A, \tag{15b}$$

$$F_2 = \kappa A \Big/ \left(\frac{1+A}{2}\frac{I_n(\kappa)}{I_n'(\kappa)} - \frac{1-A}{2}\frac{K_n(\kappa)}{K_n'(\kappa)}\right), \tag{15c}$$

$$F_3 = mA \Big/ \left(1-\frac{1-A}{2}\frac{1}{m+1}\right), \tag{15d}$$

with $\kappa \equiv kR_0$, where k is either the plane or cylindrical axial wave number. The term $s-1$ in Eq. (15a) represents the purely geometric contribution attained as $A \to 0$. It allows for certain perturbations to not grow when geometrical distortions balance exactly the pressure forces across the density interface (see Sec. II B 2). Quasiplane growth is observed when $F_s/R_0 \to KA$ as $K \to \infty$, where $K \equiv k$ for cylindrical axial perturbations, n/R_0 for cylindrical azimuthal perturbations, or m/R_0 for spherical perturbations.

2. Critical perturbations

We discuss here the theoretical existence of critical perturbations that are stable for a given implosion or explosion history. In other words, for such perturbations, for any $\dot{R}(t)$ [or $\mu(t)$], if $\dot{h}(t<0)=0$ then $\dot{h}(t>0)=0$. As a consequence, the perturbation amplitude remains fixed at h_0. Rewriting both conditions (7) and (8) at the interface for such perturbations, and integrating the second condition between $t=0^-$ and $t>0$,

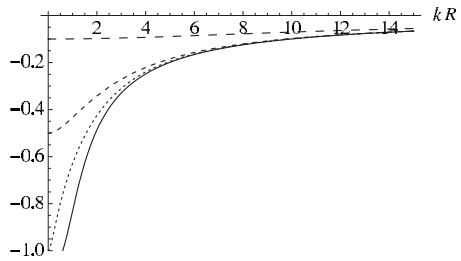

FIG. 2. Atwood ratio A_c corresponding to critical perturbations vs $kR(t)$ for $n=0$ (solid line), $n=1$ (dotted line), $n=2$ (small dashed line), and $n=10$ (dashed line).

$$\frac{\dot{R}H}{R}h_0 = g_j f_j'(R), \quad \text{for } j=1,2, \tag{16a}$$

$$Ah_0\int_{0^-}^{t}\left[\left(\frac{\dot{R}^2}{R}+\ddot{R}\right)H+\dot{R}\delta_D\right]\mathrm{d}t = \left(\frac{1-A}{2}\right)\int_{0^-}^{t} f_1(R)\dot{g}_1\mathrm{d}t - \left(\frac{1+A}{2}\right)\int_{0^-}^{t} f_2(R)\dot{g}_2\mathrm{d}t. \tag{16b}$$

Integrating by parts both integrals on the right-hand side of Eq. (16b) and using Eq. (16a) to evaluate the two resulting integrals, all integral terms cancel and, using Eqs. (9) and (11), we obtain for any t,

$$\left[kRA+\frac{1}{F(n,kR,A)}\right]\dot{R}=0. \tag{17}$$

We eliminate the trivial case $\dot{R}=0$ corresponding to a stationary interface. For a given history $R(t)$, and given n and k, critical perturbations occur only for specific values of $A_c\in[-1,1]$ given by

$$1+kRAF(n,kR,A)=0. \tag{18}$$

Equation (18) is equivalent to determining the particular Atwood ratio $A_c\in[-1,1]$ such that

$$A_c(n,kR) = \left(\frac{K_n(kR)}{K_n'(kR)}-\frac{I_n(kR)}{I_n'(kR)}\right)\Big/\left(\frac{K_n(kR)}{K_n'(kR)}+\frac{I_n(kR)}{I_n'(kR)}+2kR\right). \tag{19}$$

The variation in A_c as a function of $kR(t)$ is plotted for different values of n in Fig. 2. It is observed that critical perturbations only appear for negative A which corresponds in general to heavy-to-light shock interactions. The absolute value $|A_c|$ reaches its maximal value of 1 for a particular combination of small wave numbers, while $|A_c|$ decreases to 0 as n or kR increase. Note also that Eq. (18) is consistent with the expression (10a) in the limit $t\to 0$, $t>0$, where $kR\to kR_0\equiv\kappa$. We insist that nongrowing perturbations do not occur in plane geometry where the zero-growth condition derived from Richtmyer's impulsive growth rate is trivially $kA=0$. In the limit of purely azimuthal perturbations $kR\ll n$ with $n\geq 1$, we recover the condition $1+nA=0$ derived by Mikaelian in the case of one interface separating two cylindrical concentric shells ($N=2$ in Ref. 8).

In order to confirm numerically the prediction of Eq. (19), we would need to perform various high-resolution three-dimensional simulations whose initial conditions would cover the parametric space (k,n,M_I) at the appropriate critical Atwood ratio, and which will show minimal variation in the initial perturbation amplitude with time. The required simulations are left for future work; here we focus on light-to-heavy interactions only.

C. Effect of shock proximity

We have so far focused on the growth rate attained by small perturbations, previously denoted $\dot{h}(0^+)$, assuming that waves produced by the shock refraction are propagated instantaneously to infinity immediately following shock-interface impact. Lombardini and Pullin[13] propose a model for the effect of shock proximity on the early interface growth rate. For the case of a reflected shock, in general characterizing light-to-heavy shock interactions, they model both transmitted and reflected shocks as unperturbed boundaries (i.e., flat walls) to the linearized, impulsive, potential-flow solution, which move with speeds equal to the shock speeds obtained from the base-flow, one-dimensional Riemann problem. This results in a time-dependent growth rate

$$\frac{\dot{h}(t)}{\dot{h}_\infty}=\frac{2}{(1-A^+)\coth[KS_1(t)]+(1+A^+)\coth[-KS_2(t)]}, \tag{20}$$

where $S_1(t)$ [respectively $S_2(t)$] is the shock position of the reflected (respectively transmitted) shock evaluated in the frame of the moving interface and K is the wave number of the perturbation. From Eq. (20), a startup time, or characteristic time needed to reach an asymptotic growth-rate $\dot{h}_\infty$, was obtained as

$$\tau=\frac{1}{2k}\left(\frac{1-A^+}{U_{S_2}}+\frac{1+A^+}{(-U_{S_1})}\right). \tag{21}$$

The model aims to capture the dominant features of the growth rate evolution. The high-frequency oscillations in the growth rate are due to the reverberation of acoustic waves between the interface and the refracted receding waves and are of higher order in the approximation. Reference 13 showed satisfactory results in the plane case for a wide range of incident Mach number and gas combinations.

Assumptions are now made to apply this model, derived in the plane geometry, to converging flows. For purely axial perturbations, $K\equiv k$. For purely azimuthal perturbations, the wavelength $\lambda_\theta(t)=2\pi R(t)/n$ is time dependent. For simplicity, K will presently be identified with the initial azimuthal wave number $K\equiv n/R_0$. Since we are interested in the early-time regime where the perturbation amplitude remains small, we also assume that the shocks are moving at a constant speed U_{S_j} as in the plane case. This ignores the nonuniform nature of the flow behind the refracted diverging/converging shock waves but may be acceptable as a first-order approximation for the purpose of estimating shock-proximity effects.

The last assumption concerns the asymptotic growth rate $\dot{h}_\infty$. We define it as in the plane case by $\dot{h}_\infty \equiv \mathfrak{F}\dot{h}(0^+)$, where $\dot{h}(0^+)$ is given by Eq. (15), in which A is taken as the postshock Atwood ratio A^+ and $h(0)$ the postshock amplitude $h(0^+)$. In the weak shock limit, $\dot{h}_\infty$ tends to $\dot{h}(0^+)$. Lombardini and Pullin[13] discussed a correction for the growth rate given by Richtmyer's approach when the incident shock strength increases. For stronger shocks, such correction is difficult to capture analytically given the complex interaction between the accelerated interface and the receding waves. Lombardini and Pullin[13] suggest two directions for modeling this effect. $\mathfrak{F}$ needs to be modeled[13] or determined independently by linearized simulations.[18] Comparisons between this simplified plane-based model and compressible simulations in converging geometries for light-to-heavy interactions are made in Sec. III.

III. NUMERICAL SIMULATIONS OF THE SMALL-AMPLITUDE IMPLODING RMI

A. Numerical method and diagnostics

The simulations run on Lawrence Livermore National Laboratory machine *unclassified Purple* were conducted within the adaptive mesh refinement in oriented C++ (AMROC) framework of Deiterding,[19] based on the structured AMR algorithm by Berger and Oliger.[20] The numerical method is applied to each Cartesian subgrid of the mesh hierarchy and consists of a hybrid WENO/TCD method written for the multicomponent Euler equations assuming calorically perfect gas. The WENO scheme is used to capture discontinuities (such as shock waves) but switches to a low-numerical dissipation, explicit, center-difference scheme TCD in the smooth regions of the flow.[21,22]

Assume first purely azimuthal perturbations (no dependence on the axis coordinate z). The density interface is nominally defined by a scalar field $\psi(r,\theta,t)$, interpolated from Cartesian data onto cylindrical coordinates that asymptote to $\psi(r,\theta,t)=0$ on the light side and $\psi(r,\theta,t)=1$ on the heavy one. This is initially set up using a tanh profile (see Sec. IV A in Ref. 13). At $t>0$, we define the centerline of the smeared density interface by

$$r_c(\theta,t) \equiv \frac{\int_0^\infty r(1-\psi)\psi \mathrm{d}r}{\int_0^\infty (1-\psi)\psi \mathrm{d}r}. \tag{22}$$

The spike (heavy fluid penetrating into light fluid) and the bubble (light fluid penetrating into heavy fluid) positions $r_c=r_s$ and r_b and the flow velocity at these locations allow determination of the perturbation amplitude and growth rate as

$$h(t) = \left| \frac{r_s - r_b}{2} \right|, \tag{23a}$$

$$\dot{h}(t) = \left| \frac{u_r]_{r_s} - u_r]_{r_b}}{2} \right|. \tag{23b}$$

In order to compute the growth amplitude and rate of the spikes and bubbles, a simulation of the unperturbed system is run independently so that the position of the base interface centerline $r_u(t)$ can be calculated. We then define

$$h_s(t) = |r_s - r_u|, \quad h_b(t) = |r_b - r_u|, \tag{24a}$$

$$\dot{h}_s(t) = \left| u_r]_{r_s} - u_r]_{r_u} \right|, \quad \dot{h}_b(t) = \left| u_r]_{r_b} - u_r]_{r_u} \right|. \tag{24b}$$

In the above, we use the absolute-value function because no phase inversion is expected for light-to-heavy interactions. The same process is applied to purely axial perturbations (no dependence on θ) where, for a given z and t, the position of the interface centerline $r_c(z,t)$ is computed. To minimize the effect of grid orientations (in the case of azimuthal perturbations), we adopt high resolution in each Cartesian direction: the finest grid size is taken to be $\Delta \sim 10^{-5} R_0$ for what follows.

B. Initial conditions

1. Single converging shock

All simulations were initialized with the approximate analytical solution of Chisnell[23] that describes the full gas-dynamic flow behind a radially symmetric, imploding shock of the Guderley[24] type. Chisnell provides solutions in terms of the similarity variable $\xi=r/R_S(t)$, where the distance $R_S(t)$ of the shock from the origin at time t is given by the Guderley strong-shock approximation

$$R_S(t) = R_{S_0}\left(1 - \frac{t}{t_I}\right)^\alpha. \tag{25}$$

For a single uniform gas, the implosion time is $t_I=\alpha R_{S_0}/M_I a_0$, where M_I is the shock Mach number at $t=0$ when the shock is at $r=R_{S_0}$. The exponent $\alpha=\alpha(s,\gamma)$, where s is the space index, is determined as a nonlinear eigenvalue for the self-similar implosion.[23–29]

The density, radial velocity, and pressure fields are given by Chisnell's solution behind the incident shock at $t=0$, i.e., $r>R_{S_0}$ or $\xi_0=r/R_{S_0}>1$. The flow evolves from the initial conditions, following the Euler equations of gas dynamics. Utilizing Chisnell's converging shock solution to initialize RMI simulations has the attractive feature that it avoids spurious waves that can result from Riemann-like initial conditions and also leaves the shock thickness as the only intrinsic length scale, since the shock has no memory of when it was produced.

As a preliminary test we simulated a single self-similar, cylindrical converging shock traveling in air ($\gamma \simeq 1.40$). At $t=0$, $M_I=3.0$ at $R_{S_0}=R_0$. The grid size Δ is then the only length scale. The circularity of the shock was evaluated as it converges to the axis where it reflects as an expanding shock. The eccentricity of both imploding and exploding shocks remains less than 0.2%. The self-similar structure of the flow behind the shock has also been observed down to small radial positions of the shock front. Figure 3 shows a satisfactory agreement between the shock position obtained from the present simulation and Guderley's self-similar solution.[24] The exponent α was determined using a three-parameter least-squares fit of the form $R_{S_0}(1-t/t_I)^\alpha$ for the imploding shock [cf. Eq. (25)] and $R_S^E(t/t_I-1)^{\alpha^E}$ for the exploding

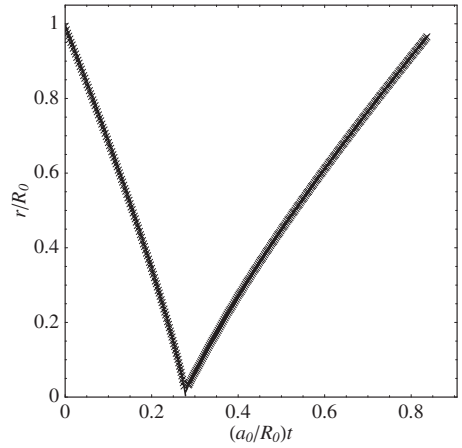

FIG. 3. Imploding and exploding shock front average radial positions r/R_0 vs $(a_0/R_0)t$. The converging shock travels in air with Mach number of 3.0 at $r=R_0$. Superposition of two-dimensional simulation results of cylindrical shock initialized by Chisnell's solution (crosses) and a power-law least-squares fit for both imploding and exploding shocks (solid line).

shock. Table I compares these with values obtained from the nonlinear eigenvalue problem,[23–29] which predicts that $\alpha^E=\alpha$. Additional validation has been performed in Ref. 30 where successful comparisons have been made between Cartesian-mesh based computations using AMROC and experiments of shock focusing on planar shock wave propagating into a linearly convergent wedge.

2. Parameters of the shock-contact interaction

A converging shock traveling in air now impacts at $t=0$ an air/SF_6 interface located at $r=R_0$. The ratios of specific heats for these gases are $\gamma_1\equiv\gamma_{\text{air}}=1.40$ and $\gamma_2\equiv\gamma_{SF_6}=1.09$. The preshock Atwood ratio is chosen such that the temperature is continuous across the initial interface, which is consistent with experimental conditions. For the gas combination chosen, $A=0.67$, for which the effects of shock proximity are expected to be important. The preshock perturbation amplitude h_0 is taken sufficiently small compared with the initial perturbation wavelength in order to remain in the linear regime as long as possible $[h(t)\ll 2\pi/K]$. The parameters are the incident shock Mach number M_I immediately before shock-interface impact and the perturbation wave numbers. Table II summarizes the various runs performed in plane, cylindrical, and axisymmetric spherical geometries with an emphasis on the cylindrical case. Figure 4 shows various implosion histories obtained from simulations of a shock impacting an unperturbed interface. In the plane geometry, the shocked interface moves at a constant speed ΔW. In curved geometries, the interface accelerates increasingly as it converges toward the axis/center $r=0$. After the transmitted shock reflects off the axis/center, reshock follows. This limits the time range of the current study. The dimensionless reshock time $(a_0/R_0)t_{\text{res}}$ is bounded between the implosion time $(a_0/R_0)t_I=\alpha/M_I$, and the time at which the interface would reach $r=0$ if there was no reshock, which is approximately $a_0/\Delta W$ if we neglect the acceleration of the interface.

TABLE I. Three-parameter least-squares fit for imploding and exploding shocks.

Imploding shock	R_{S_0}/R_0	$(a_0/R_0)t_I$	α
Exact	1.000	0.27844	0.83532
Best fit	0.995	0.278	0.8354
Exploding shock	R_S^E/R_0	$(a_0/R_0)t_I$	α^E
Exact	⋯	0.27844	0.83532
Best fit	0.533	0.278	0.8355

IV. RESULTS FOR THE SMALL-AMPLITUDE IMPLODING RMI

We choose $1/(a_0K)$ as the reference time scale for data representation, where a_0 is the speed of sound in the region $j=1$ ahead of the incident shock and K is the perturbation wave number ($K=k$ for purely axial modes and n/R_0 for purely azimuthal modes). This is the simplest intuitive time scale that is independent of M_I and A. The reference scale for the interface, spike, and bubble computed amplitudes is taken as the preshock amplitude h_0, while the asymptotic growth rate $\dot{h}_\infty$ (cf. Sec. II C) is used to make dimensionless the interface, spike, and bubble growth rates obtained from the simulations. We insist that because $\dot{h}_\infty$ depends on M_I and the wave numbers (for A fixed), two numerical results obtained from varying one of these parameters will then be made dimensionless by a different value of $\dot{h}_\infty$. Therefore, care has to be used when comparing quantitatively growth rates related to distinct K or M_I on the same plot. We recall the dependencies $\dot{h}_\infty\simeq\mathfrak{F}_{(M_I)}\dot{h}(0^+)_{(K,M_I)}$ with $\mathfrak{F}_{(1.2,2.0,3.0)}=(1.02,0.85,0.71)$ (from Ref. 18) and

$$\dot{h}(0^+)_{(K,M_I)}=\frac{h(0^+)_{(M_I)}}{R_0}\Delta W_{(M_I)}[1+KR_0A^+_{(M_I)}]. \tag{26}$$

Note also that the model for $\dot{h}/\dot{h}_\infty$ given by Eq. (20) and plotted (together with the numerical results) as a function of the dimensionless time a_0Kt depends only on M_I through the values of A^+ and the shock velocities U_{S_j}.

A. Purely axial perturbations

The initial flow is considered axisymmetric and the interface is described by

$$r_c(z,t<0)=R_0+h_0\cos(kz). \tag{27}$$

Two-dimensional simulations are performed in a plane (r,z) with given azimuthal orientation θ. Geometric source terms are added to the right-hand side of the Euler equations to take into account the axisymmetry of the flow.[31] In this configuration, the main effect of the geometry on the perturbation evolution is due to the acceleration of the flow toward the axis. As for the plane case, the wavelength of the perturbation $2\pi/k$ remains constant with time. The influence of k and M_I is investigated.

We report first the influence of the axial wave number k of a material interface impacted by a $M_I=1.2$ shock. Figure 5 shows the amplitudes and growth rates of the interface per-

TABLE II. Table of runs for an air→SF_6 ($A=0.67$) shock interaction with single mode perturbations of initial amplitude $h_0/R_0=0.005$. $a_0K\tau$ is computed using Eq. (22) in Ref. 13, while $\dot{h}(0^+)/a_0$ is obtained from Eq. (15). Postshock amplitude and Atwood ratio $h(0^+)$, A^+ and interface velocity ΔW are evaluated from the simulation immediately following the shock interaction and depend on the incident shock strength only.

Geometry	M_I	wave number KR_0	A^+	$h(0^+)/R_0$	$\Delta W/a_0$	$a_0K\tau$	$\dot{h}(0^+)/a_0$
Plane	1.2	$kR_0=24$	0.700	0.0042	0.202	2.896	0.0157
	1.2	$kR_0=8$	0.700	0.0042	0.202	2.896	0.0062
	1.2	$kR_0=16$	0.700	0.0042	0.202	2.896	0.0114
	1.2	$kR_0=24$	0.700	0.0042	0.202	2.896	0.0167
Cylindrical axial ($n=0$)	1.2	$kR_0=32$	0.700	0.0042	0.202	2.896	0.0219
	1.2	$kR_0=40$	0.700	0.0042	0.202	2.896	0.0271
	2.0	$kR_0=32$	0.766	0.0030	0.828	4.792	0.0634
	3.0	$kR_0=32$	0.801	0.0026	1.498	5.700	0.1046
	1.2	$n=8$	0.700	0.0042	0.202	2.896	0.0062
	1.2	$n=12$	0.700	0.0042	0.202	2.896	0.0088
	1.2	$n=16$	0.700	0.0042	0.202	2.896	0.0115
Cylindrical azimuthal ($k=0$)	1.2	$n=24$	0.700	0.0042	0.202	2.896	0.0167
	1.2	$n=36$	0.700	0.0042	0.202	2.896	0.0246
	2.0	$n=36$	0.766	0.0030	0.828	4.792	0.0714
	3.0	$n=36$	0.801	0.0026	1.498	5.700	0.1179
Spherical azimuthal (axisymmetric)	1.2	$m=24$	0.70	0.0042	0.202	2.896	0.0176

turbation, spikes, and bubbles as a function of time. Figures 5(a) and 5(b) show that the plane-based model given by Eq. (20) qualitatively agrees with the numerical results obtained for various k. The growth rate reaches the asymptotic level $\dot{h}_\infty$ with a characteristic time scale comparable to τ given by Eq. (21). The satisfactory agreement is partly due to the low incident Mach number used resulting in (i) the amplitude to remain small compared with the wavelength and (ii) the interface to converge less rapidly toward the axis, therefore reducing acceleration effects.

For smaller k, the growth is slower and the reshock occurs earlier in the growth evolution. Inversely, for higher k, the growth is faster, allowing for a longer evolution of the perturbation before reshock. The oscillatory aspect of the computed growth rates of the material interface, spikes, and bubbles is a compressible effect produced by the reverberation of transverse waves traveling between the perturbed interface and the distorted shocks. This effect should then depend on the distance shocks/interface, i.e., the shock speeds U_{S_j} (invariant here as M_I is fixed), and the distortion of the refracted waves, which is k. Right-hand side subfigures of Fig. 5 show that the oscillatory nature of the growth roughly scales like constant times kt. Unlike the spike structure, the bubble growth rates exhibit a slow but continuous decrease at late times, characteristic of the emergence of nonlinear growth. Higher wave number modes, which grow faster compared with the contraction of the interface, are more affected by this late-time decrease.

The incident Mach number influences the evolution of the perturbation growth in various ways. First, the deposition of baroclinic vorticity is naturally more important after the passage of stronger shocks. This results in a more intense growth and consequently the onset of nonlinear effects earlier than for weaker shocks, leading to a progressive slowdown in the evolution of the growth. Second, for light-to-heavy configurations, compressible interactions between the accelerated interface and the transmitted shock intensify at higher M_I since interface and transmitted shock evolve closer to each other during their convergence toward the axis. This effect should contribute to limit the linear growth. Third, since the interface accelerates toward the axis, the flow is Rayleigh–Taylor unstable during the implosion phase. This effect is logically increased for stronger incident shocks. As we increase the incident Mach number for a fixed wave number, we first observe from Fig. 6 that Eq. (20) does not capture the evolution of the linear growth for strong shocks

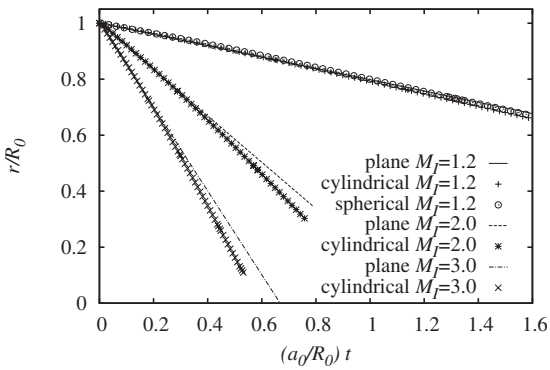

FIG. 4. Postshock interface base radial position $R(t)/R_0$ vs $(a_0/R_0)t$ in plane and converging geometries for various M_I. An incident shock impacts the density interface at rest at $t=0$ with an instantaneous Mach number M_I.

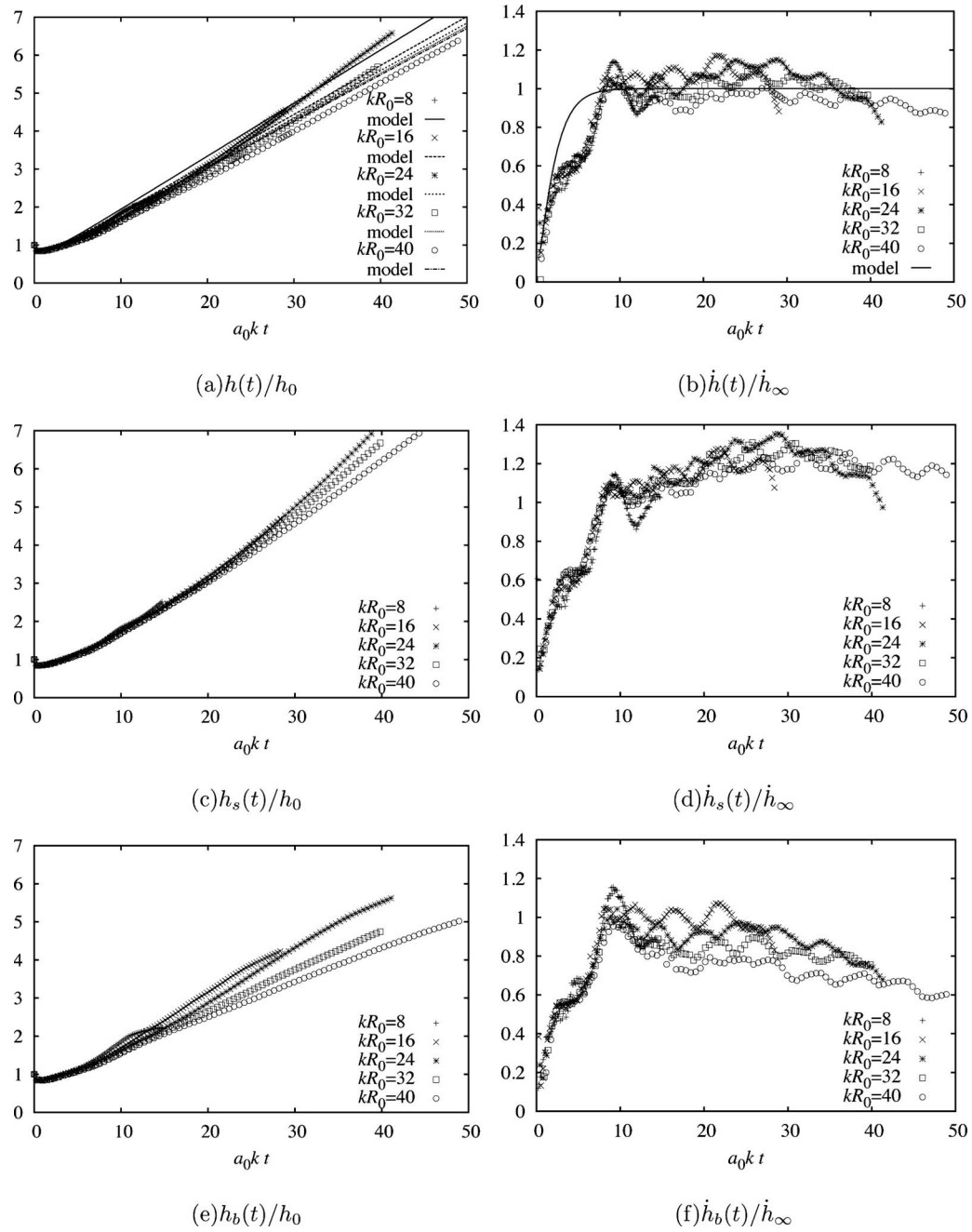

FIG. 5. Axial perturbations ($n=0$): dimensionless amplitude (left) and growth rate (right) vs a_0kt of the interface perturbation (top), spike front (middle), and bubble front (bottom) plotted for different k; case air$\rightarrow$$SF_6$, $h_0/R_0=0.005$, $M_I=1.2$. See details in Sec. III B 2.

because the previously cited effects are not correctly modeled in curved geometries. Our treatment of the shock proximity effect[13] assumes that both refracted waves were traveling at constant speed, which is not the case here. The simulations show that for higher incident shock strengths, the growth accelerates as long as the amplitude of the instability remains small and the reshock has not occurred yet. The Mach number influence is mainly visible on the spike growth rate plots, unlike the bubble growth rate.

To appreciate the underlying influence of the converging geometry on the growth of the instability, specially at higher Mach numbers, we consider the volume of fluid $V_{\mathrm{cyl}}(t)$ contained between the spike and bubble cylindrical radii in place of the width of the perturbation. As $r_s > r_b$ for a light-to-heavy interaction,

$$V_{\mathrm{cyl}}(t) = L_z(\pi r_s^2 - \pi r_b^2) = 2\pi L_z h\left(r_u + \frac{h_s - h_b}{2}\right), \tag{28}$$

which summarizes the competition between the growth of the perturbation amplitude $h(t)$ and the convergence of the interface $r_u(t)$. In practice, for small perturbations, $V_{\mathrm{cyl}} \sim h(t)R(t)$. In addition, we introduce in a simple way the dependence on M_I through the mass $\rho_{0'}V(t)$, where $\rho_{0'}$ is the

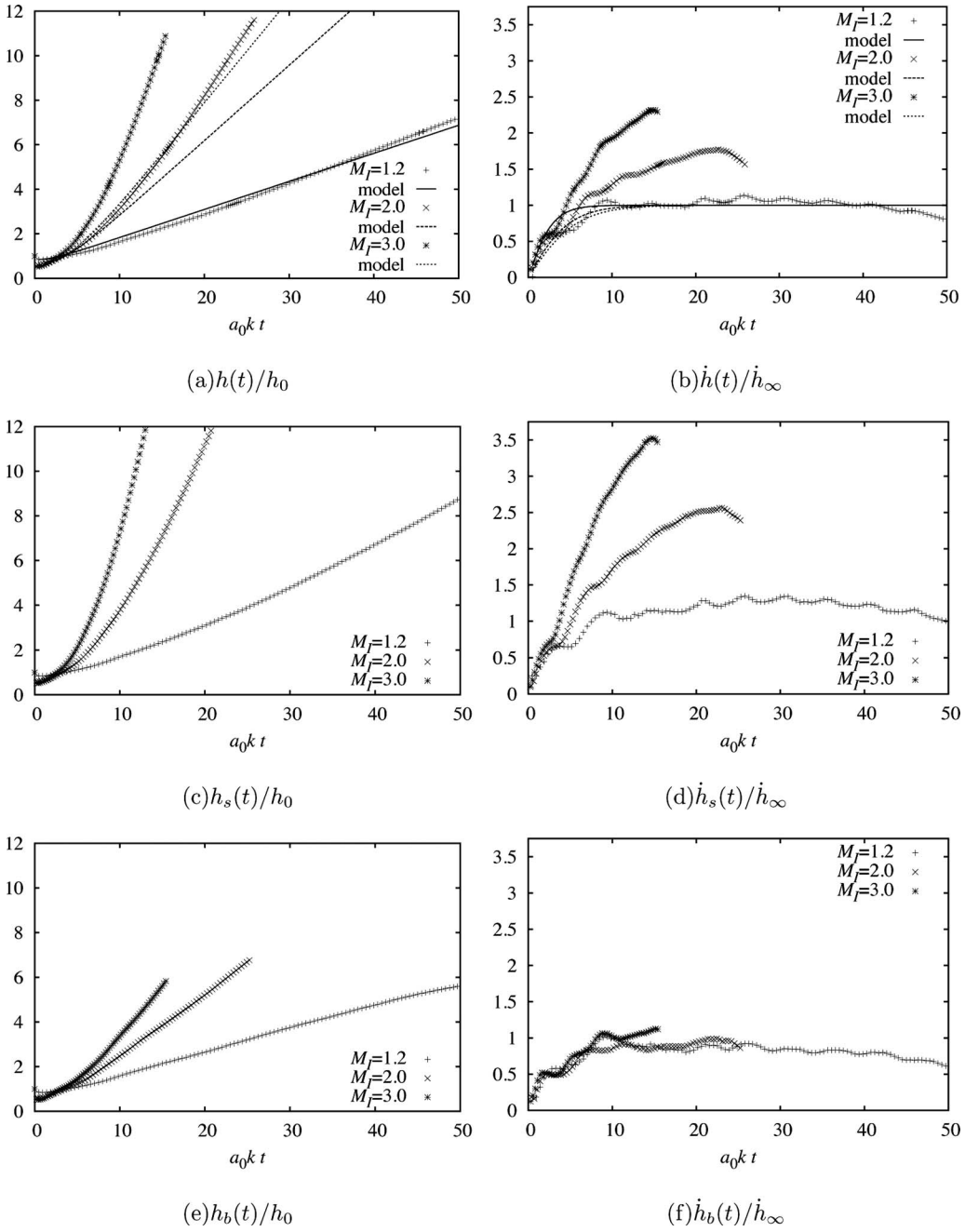

FIG. 6. Axial perturbations ($n=0$): dimensionless amplitude (left) and growth rate (right) vs a_0kt of the interface perturbation (top), spike front (middle), and bubble front (bottom) plotted for three different M_I; case air$\rightarrow$SF$_6$, $h_0/R_0=0.005$, $kR_0=32$. See details in Sec. III B 2.

density just behind the incident shock at $t=0^-$ defined as

$$\rho_{0'} = \rho_0 M_I^2 \Bigg/ \left[1 + \frac{\gamma_1 - 1}{\gamma_1 + 1}(M_I^2 - 1)\right]. \tag{29}$$

The top left subfigure of Fig. 7 represents the dimensionless volumes (in fact masses) $\rho_{0'}V/(\rho_0 R_0^3)$ related to the growth of the cylindrical layer as a function of the convergence ratio $R(t)/R_0$. The top right subfigure shows the corresponding dimensionless volume growth rates $\rho_{0'}\dot{V}/[-\dot{R}(0^+)\rho_0 R_0^2]$ versus $R(t)/R_0$. Similar dimensionless quantities are defined to characterize the spike and bubble growths: the volume of perturbed fluid is now contained between two cylindrical surfaces corresponding to either r_s or r_b in the perturbed configuration and the unperturbed interface radial position r_u. Results are represented in the middle and bottom subfigures of Fig. 7. For each M_I, the right subfigures of Fig. 7 show two distinct phases, which were not distinguishable with the representation of Fig. 6. The first phase corresponds to early-time increase in the volume growth rate of the cylindrical layer due to the instability growth. In a second phase, the volume growth rate starts decreasing as an effect of the geometric convergence. The late-time volume growths of the interface, spikes, and bubbles are characterized by a decay of the dimensionless volume growth rate almost independent of the convergence ratio $R(t)/R_0$ and quasi-independent of M_I at the given axial wave number considered. This can be

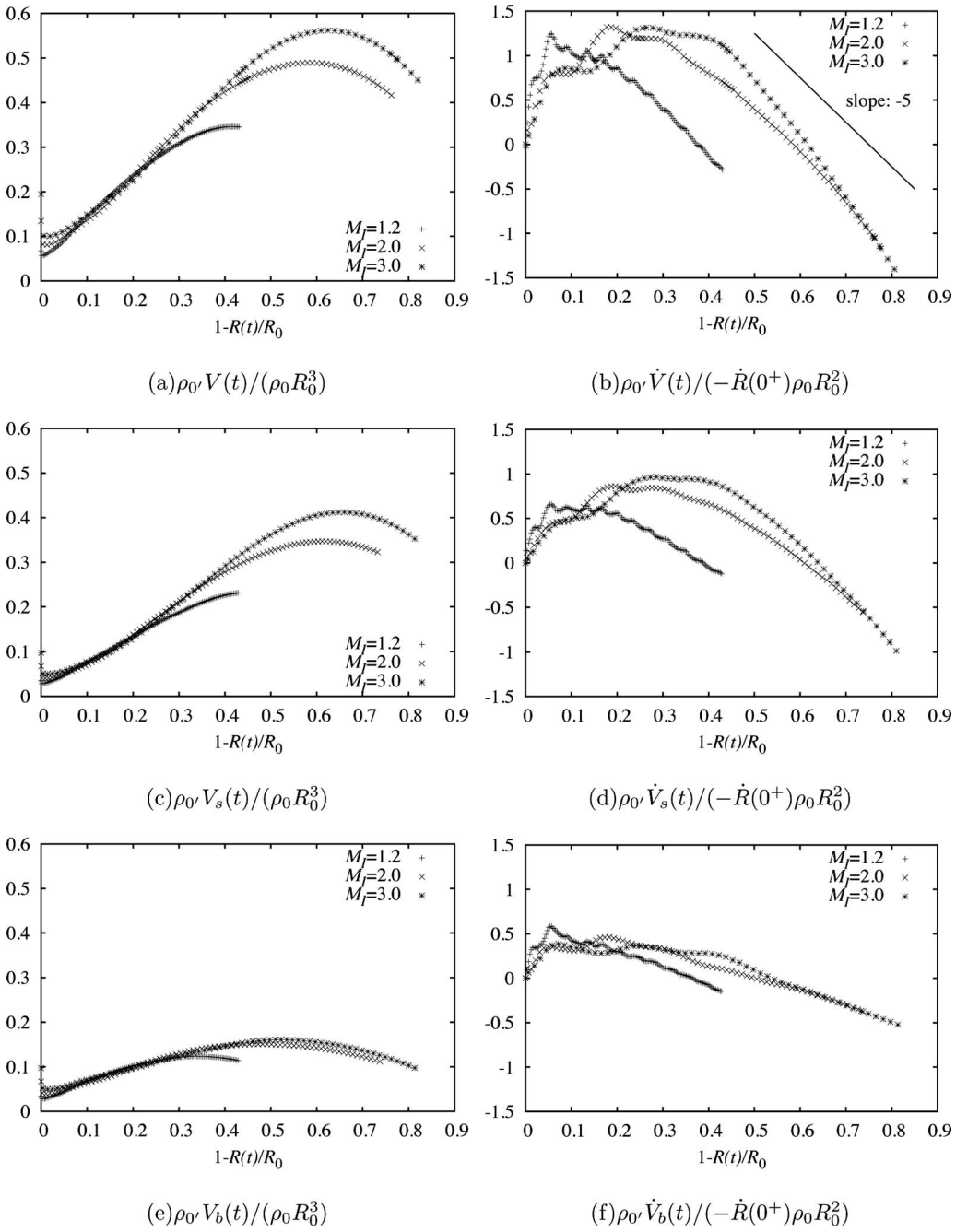

FIG. 7. Axial perturbations ($n=0$): dimensionless volume (left) and volume growth rate (right) vs $1-R(t)/R_0$ of the interface perturbation (top), spike front (middle), and bubble front (bottom) plotted for three different M_I; case air→SF_6, $h_0/R_0=0.005$, $kR_0=32$. See details in Sec. III B 2.

translated in terms of the deceleration $\ddot{V}$: for example, the late-time deceleration of the interface volume growth is

$$\frac{\rho_{0'}}{\rho_0}\frac{1}{\dot{R}(0^+)^2 R_0}\ddot{V} \sim -5\frac{\dot{R}}{\dot{R}(0^+)}. \tag{30}$$

We know of no theoretical work that estimates the late-time decay of the volume growth rate in converging geometries. As a result of the volume growth rate decay, at higher M_I, the volumes stop growing and ultimately start decaying, as observed in the left subfigures of Fig. 7, while the perturbation amplitudes themselves continue growing (left subfigures of Fig. 6).

B. Purely azimuthal perturbations

We consider now zero axial perturbation

$$r_c(\theta, t<0) = R_0 + h_0\cos(n\theta). \tag{31}$$

Two-dimensional simulations are performed in a polar plane (r,θ) with fixed axial coordinate z, and the influence of n as well as M_I is investigated. Two geometrical effects are present in this case: the acceleration of the flow toward the origin, like in the axial case, and the geometric curvature as the azimuthal wavelength decreases during the implosion (the mode number n being invariant).

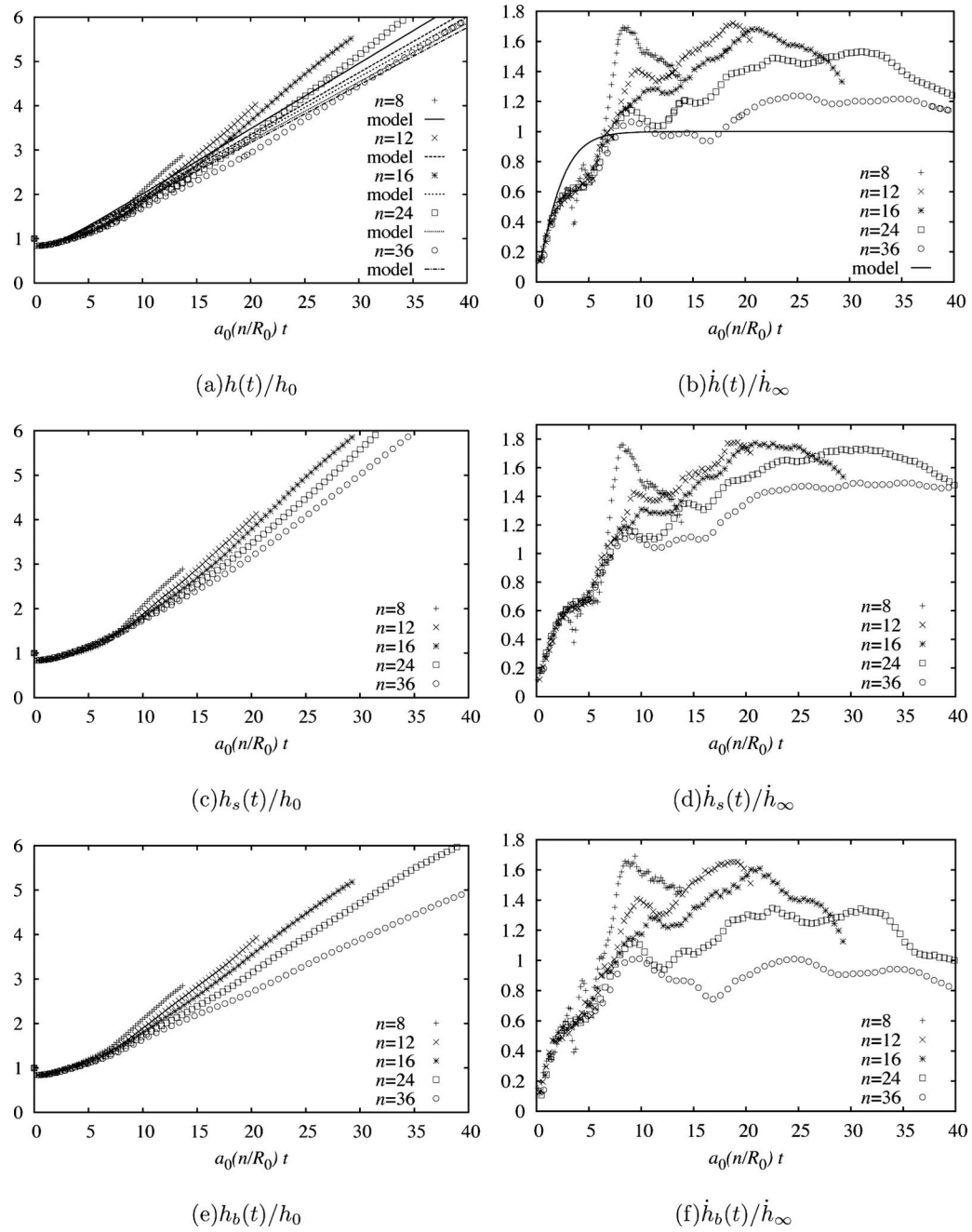

FIG. 8. Azimuthal perturbations ($k=0$): dimensionless amplitude (left) and growth rate (right) vs $a_0(n/R_0)t$ of the interface perturbation (top), spike front (middle), and bubble front (bottom) plotted for different n; case air$\rightarrow$SF$_6$, $h_0/R_0=0.005$, $M_I=1.2$. See details in Sec. III B 2.

We compare various azimuthal modes for $M_I=1.2$. As shown in Figs. 8(a) and 8(b), the early time evolution of the linear regime is similar to the one observed in the plane case with a characteristic time τ. For higher n, the growth rate reaches a plateau, comparable to the theoretical prediction $\dot{h}_\infty$. This behavior is similar to the plane geometry because (i) the initial perturbation does not see the curvature of the interface $[\lambda_\theta(t=0) \ll 2\pi R_0]$; (ii) as the perturbation grows faster, the interface has not converged sufficiently to feel the effects of curvature and acceleration $[\lambda_\theta(t) \ll 2\pi R(t)]$. The converging nature of the flow influences smaller azimuthal wave numbers. As a result of the geometry—RTI due to flow acceleration, and instantaneous wave number $n/R(t)$ increasing with time—the growth rate is stronger in comparison to plane instability with equivalent initial perturbation wavelength ($\dot{h}$ significantly higher than the plane-based asymptotic level $\dot{h}_\infty$). At later time, as the instantaneous perturbation wavelength becomes comparable to the interface length $2\pi R(t)$, the perturbation enters nonlinear regime and the growth rates start decaying, specially for the bubble structures. The growth rate plots on the right-hand side present a moderately oscillatory behavior compared with the axial and plane geometries. This suggests that the dynamics

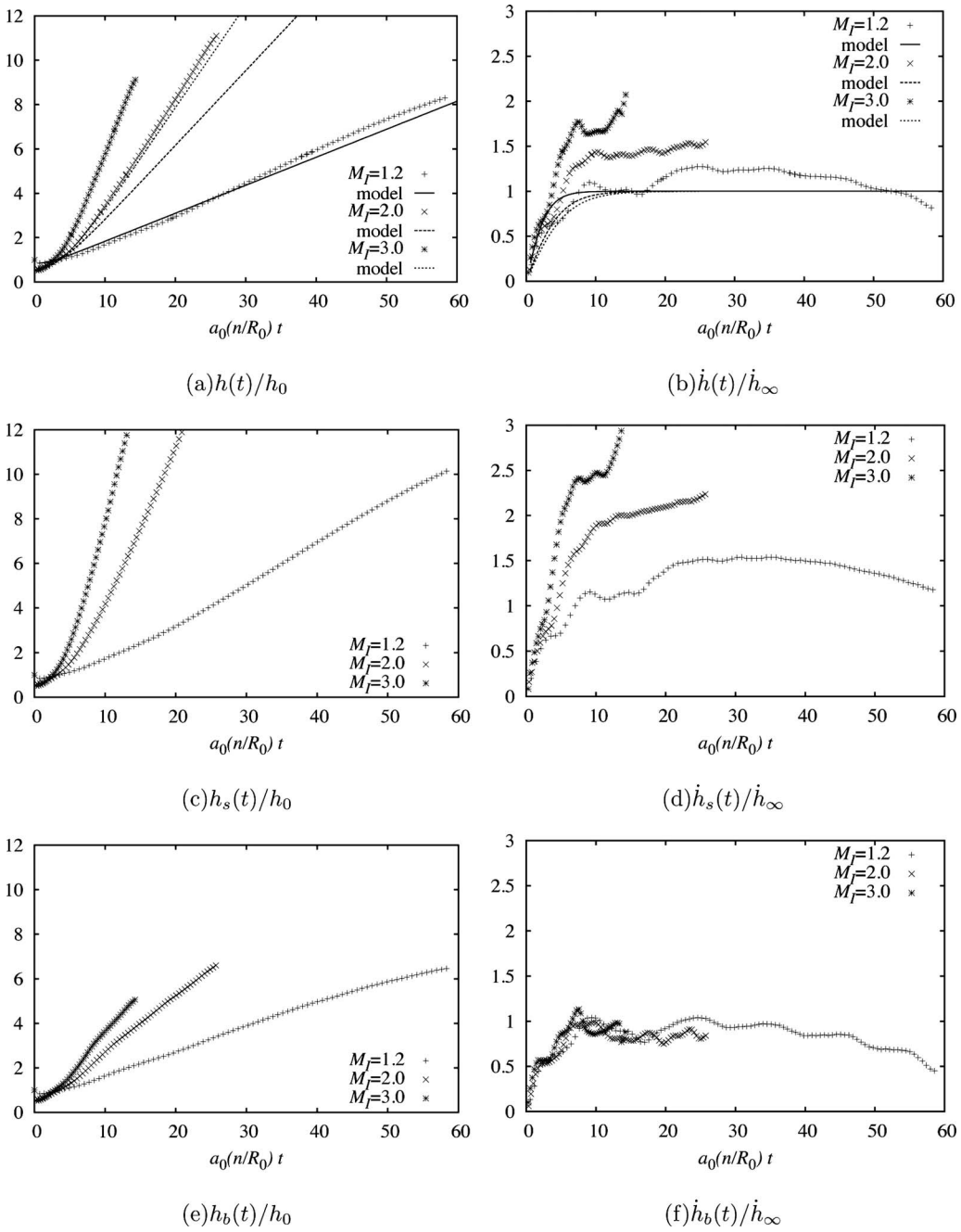

FIG. 9. Azimuthal perturbations (k=0): dimensionless amplitude (left) and growth rate (right) vs $a_0(n/R_0)t$ of the interface perturbation (top), spike front (middle), and bubble front (bottom) plotted for three different M_I; case air→SF_6, h_0/R_0=0.005, n=36. See details in Sec. III B 2.

of azimuthal shock front distortions, responsible for these high-frequency changes in the growth rates, differs to that of plane distortions typical of plane or axial geometries.

We now consider variations in M_I with high wave number n=36 in order to minimize the effect of the curvature (Fig. 9). As M_I increases, convergence effects responsible for the acceleration of the linear growth have a more significant influence. Our model for the asymptotic behavior of the growth underestimates the actual growth because the acceleration of the flow and the curvature of the shock and contact waves are not modeled.

As for purely axial perturbations, Fig. 10 allows us to distinguish two different phases in the volume growth of the cylindrical layer. At early time, the volume growth rate increases and the volume grows. The late-time evolution of the layer is characterized by a decay in the growth rate, which results in a decrease in the volume at higher M_I when high convergence ratios are reached. As for axial perturbation, for a given azimuthal wave number, the late-time volume growths of the interface, spikes, and bubbles are characterized by a decay of the dimensionless volume growth rate almost independent of the convergence ratio $R(t)/R_0$ and quasi-independent of M_I. The late-time deceleration of the interface volume growth can be approximated by Eq. (30).

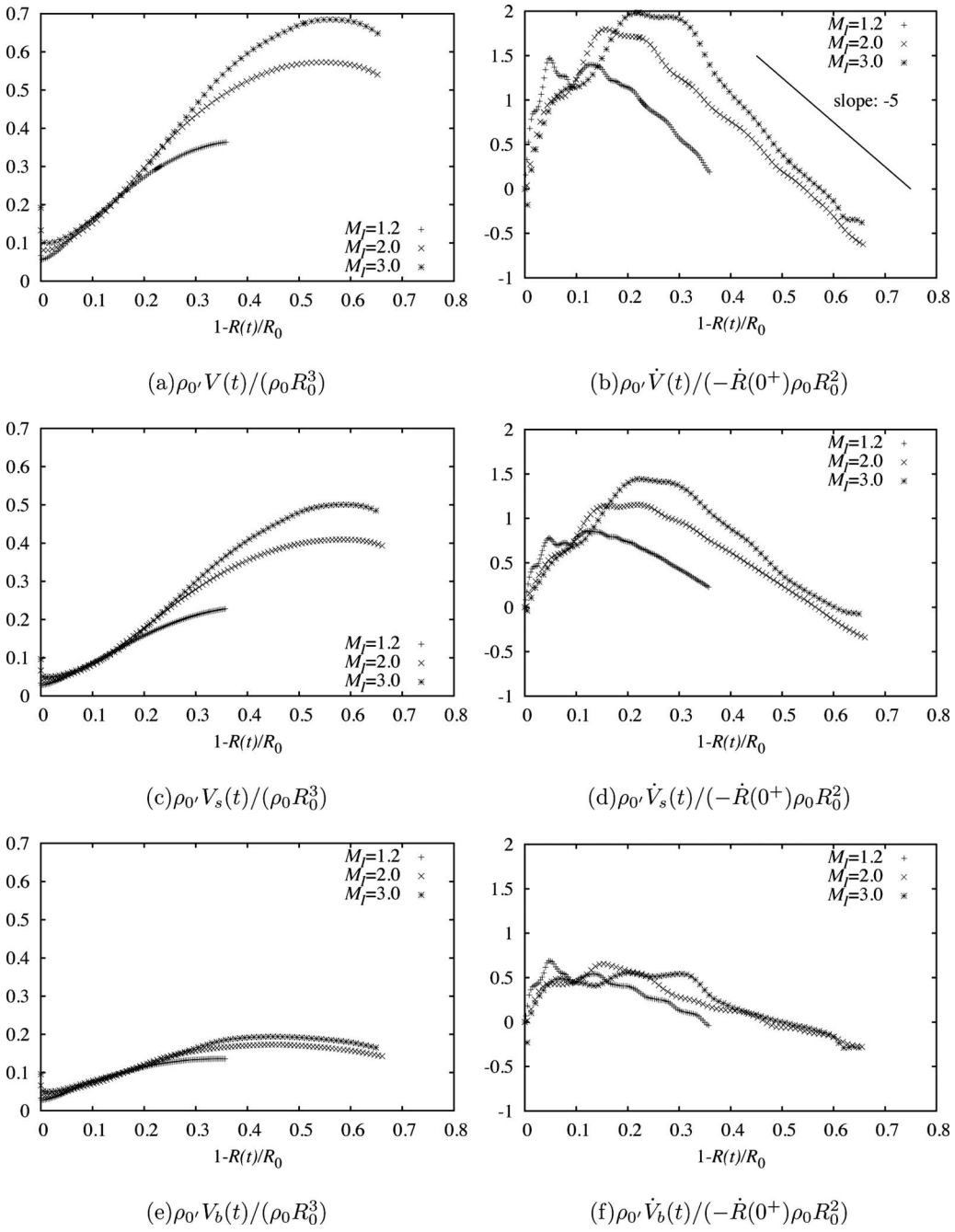

FIG. 10. Azimuthal perturbations ($k=0$): dimensionless volume (left) and volume growth rate (right) vs $1-R(t)/R_0$ of the interface perturbation (top), spike front (middle), and bubble front (bottom) plotted for three different M_I; case air$\rightarrow$SF$_6$, $h_0/R_0=0.005$, $n=36$. See details in Sec. III B 2.

C. Comparison between plane, cylindrical, and spherical geometries

Both axial and azimuthal perturbation growths are compared with the growth in plane and spherical geometries by choosing the same equivalent initial wavelength KR_0 and amplitude h_0/R_0, just preceding the shock interaction. We consider here the additional case of an axisymmetric spherical flow driven by a spherical converging self-similar shock given by Chisnell.[23] The perturbed interface is given in any plane (r,z) by the azimuthal form

$$\rho_c(\phi,t<0)=R_0+h_0\cos(m\phi), \tag{32}$$

where $\rho=\sqrt{r^2+z^2}$ and $\phi=\arctan(r/z)$. As for the axial cylindrical geometry, such axisymmetric flow can be solved two dimensionally using appropriate geometric source terms. The diagnostics are similar to those for the cylindrical azimuthal perturbations and follow from the changes $r\leftrightarrow\rho$ and $\theta\leftrightarrow\pi/2-\phi$. For each geometry, the Mach number of the incident shock just before interaction with the interface is set to $M_I=1.2$.

Some of the earlier discussions comparing plane with curved geometry are well summarized in Fig. 11. It first demonstrates that at very early times in the linear regime, plane and curved geometries agree well as $R(t)$ is still close

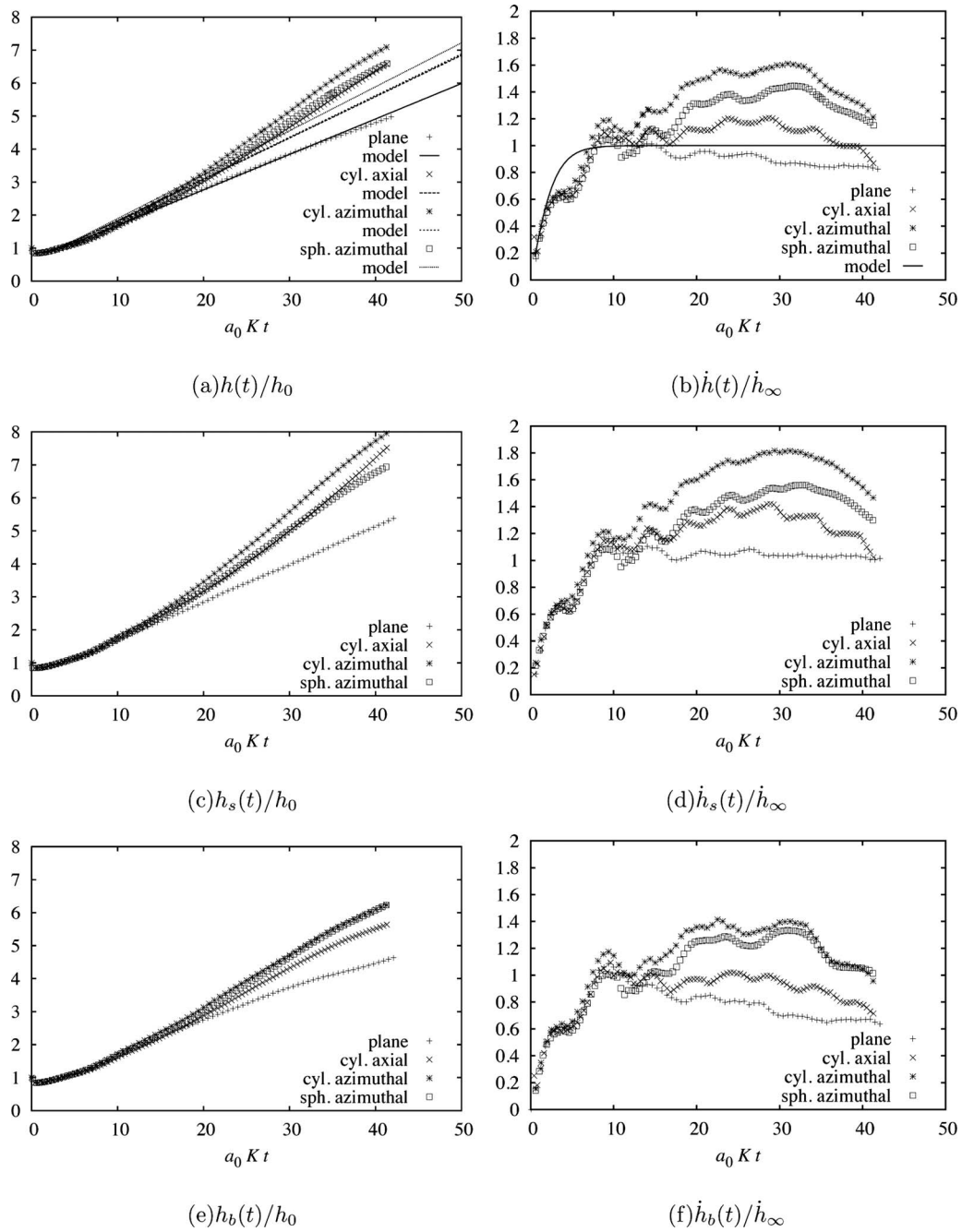

FIG. 11. Dimensionless amplitude (left) and growth rate (right) vs a_0Kt of the interface perturbation (top), spike front (middle), and bubble front (bottom) plotted for the plane, cylindrical axial, cylindrical azimuthal, and spherical azimuthal perturbations; case air$\rightarrow$SF$_6$, M_I=1.2, Kh_0=0.12; for the plane geometry $KR_0 \equiv kR_0$=24, for cylindrical axial geometry h_0/R_0=0.005 and $KR_0 \equiv kR_0$=24, the azimuthal geometry h_0/R_0=0.005 and $KR_0 \equiv n$=24, and the spherical azimuthal geometry h_0/R_0=0.005 and $KR_0 \equiv m$=24. See details in Sec. III B 2.

to R_0. However, the growths of the interface perturbation, spikes, and bubbles are evolving faster and the amplitudes attained are consequently higher for curved geometries than for the plane one, until late times when nonlinear regime starts taking place. This characteristic slowdown is observed on the growth rates represented on the right subfigures of Fig. 11.

If we define the geometric factor[8,11] $G=h_{\text{curved}}/h_{\text{plane}}$, we observed $G>1$. Similar observations have been made in the single-mode incompressible RTI experiments of imploding gelatin rings by Weir *et al.*[32] From Fig. 11, we remark inparticular that for the interface, spikes, and bubbles, and at all time,

$$h_{\text{cyl azim}} \gtrsim h_{\text{sph azim}} \gtrsim h_{\text{cyl axial}} \gtrsim h_{\text{plane}}, \tag{33a}$$

$$\dot{h}_{\text{cyl azim}} \gtrsim \dot{h}_{\text{sph azim}} \gtrsim \dot{h}_{\text{cyl axial}} \gtrsim \dot{h}_{\text{plane}}, \tag{33b}$$

$$h_{s,b\text{–cyl azim}} \gtrsim h_{s,b\text{–sph azim}} \gtrsim h_{s,b\text{–cyl axial}} \gtrsim h_{s,b\text{–plane}}, \tag{33c}$$

$$\dot{h}_{s,b\text{–cyl azim}} \gtrsim \dot{h}_{s,b\text{–sph azim}} \gtrsim \dot{h}_{s,b\text{–cyl axial}} \gtrsim \dot{h}_{s,b\text{–plane}}. \tag{33d}$$

This indicates that plane, axial, and azimuthal converging geometries exhibit an increasingly high growth in this order.

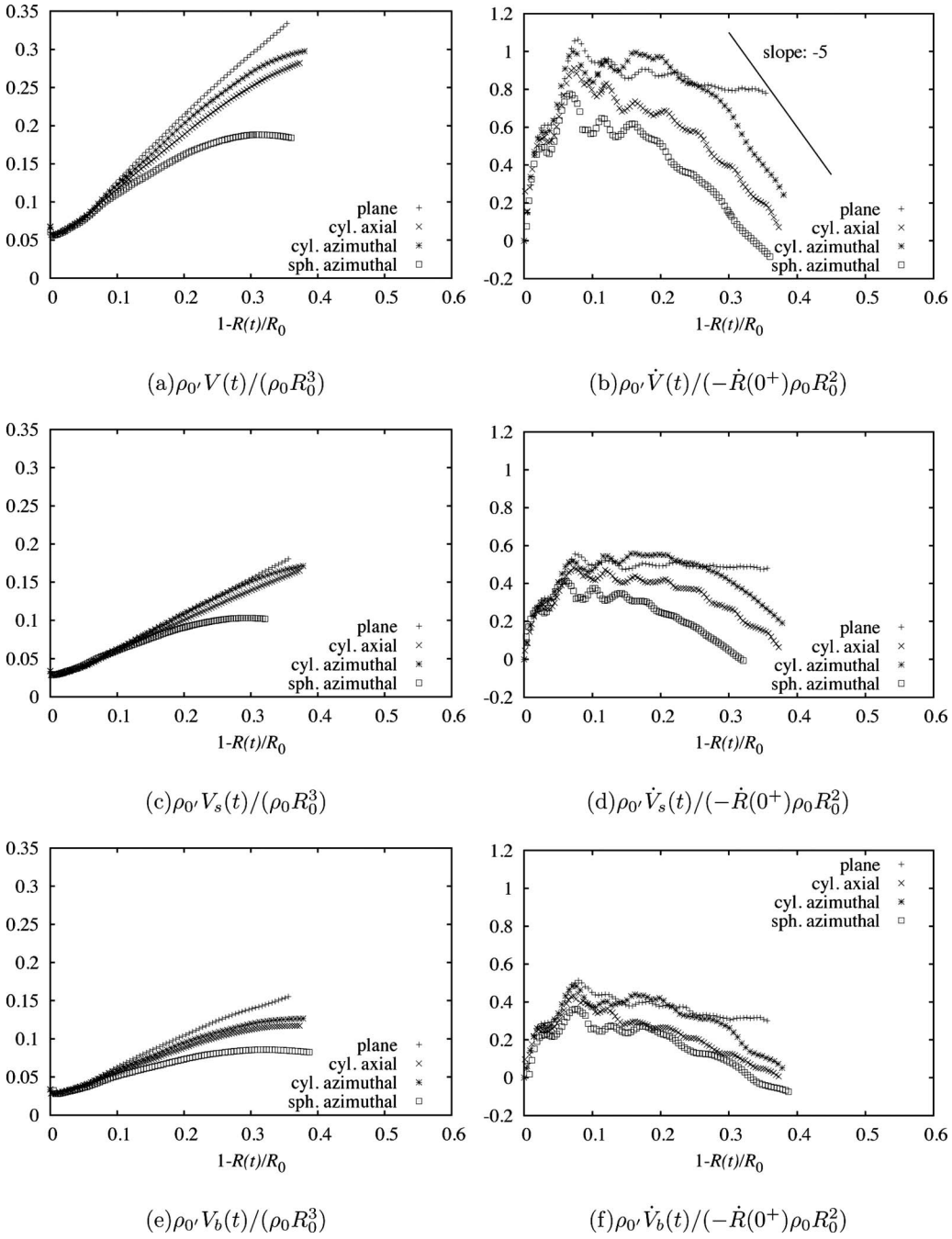

FIG. 12. Dimensionless volume (left) and volume growth rate (right) vs $1-R(t)/R_0$ of the interface perturbation (top), spike front (middle), and bubble front (bottom) plotted for the plane, cylindrical axial, cylindrical azimuthal, and spherical azimuthal perturbations; case air→SF_6, $M_I=1.2$, $Kh_0=0.12$; for the plane geometry $KR_0 \equiv kR_0=24$, for cylindrical axial geometry $h_0/R_0=0.005$ and $KR_0 \equiv kR_0=24$, the azimuthal geometry $h_0/R_0=0.005$ and $KR_0 \equiv n=24$, and the spherical azimuthal geometry $h_0/R_0=0.005$ and $KR_0 \equiv m=24$. See details in Sec. III B 2.

It is not clear, however, what differentiates the growth of cylindrical and spherical azimuthal modes, for which the instantaneous perturbation wave numbers both vary as $KR_0/R(t)$. Moreover, at such low M_I the implosion histories are very similar (cf. Fig. 4). Therefore, the main distinction between these two configurations is simply a different geometrical constraint: in the cylindrical configuration, the azimuthal mode is decorrelated from the axial flow (invariance in the axial direction); in the spherical geometry, azimuthal perturbations are constrained by the axisymmetry of the configuration. From Fig. 11(e), identical behavior is observed for the bubble evolution of both cylindrical and spherical azimuthal geometries, but a difference is observed in the spike evolutions in Fig. 11(c). Figure 11(c) shows that the spike evolution is very similar for both axisymmetric configurations (cylindrical axial and spherical azimuthal geometries).

We represent in Fig. 12 the volume growths of the perturbation in plane, cylindrical, and spherical geometries after defining

$$V_{\text{plane}}(t) = 2\pi R_0 L_z (r_s - r_b), \tag{34a}$$

$$V_{\text{sph}}(t) = \frac{4\pi}{3}(r_s^3 - r_b^3)\frac{L_z}{2R_0}. \tag{34b}$$

For proper comparison, both volumes were defined up to a constant factor chosen, such that at $t=0$, they match the initial volume of the cylindrical layer $\sim 2\pi R_0 L_z h_0$. Note for example that $V_{\text{cyl}}(t)/V_{\text{plane}}(t) \sim G(t)R(t)/R_0$. Similar definitions hold for the spike and bubble volumes. As mentioned in the cylindrical perturbations tested at various M_I, Fig. 12 shows two phases in the volume growth of the layer in curved
geometries: (i) increase in the growth rate at early times due to the instability and (ii) strong decay in the growth rate at later times due to convergence while the plane growth rate remains stationary. The difference among the three curved geometries is not noticeable at early times as the convergence ratio is still low, but for increasing space index and for a given couple (M_I, K), at all time,

$$V_{\text{plane}} \gtrsim V_{\text{cyl}} \gtrsim V_{\text{sph}}, \tag{35a}$$

$$\dot{V}_{\text{plane}} \gtrsim \dot{V}_{\text{cyl}} \gtrsim \dot{V}_{\text{sph}}. \tag{35b}$$

As a last observation on the growth in curved geometries, given the initial wave number and Mach number [$\rho_{0'}$ and $\dot{R}(0^+)$ fixed], the late-time volume growths of the interface, spikes, and bubbles are characterized by a decay of the dimensionless volume growth rate almost independent of the convergence ratio $R(t)/R_0$ (modulo some high-frequency oscillations) and independent of the curved geometry. For each curved geometry, an approximation for the late-time deceleration of the interface volume growth is given by Eq. (30).

V. CONCLUSION

An extension of Mikaelian's theory to three-dimensional perturbations for the linear growth of the cylindrical RMI has been developed. Limit cases have been discussed, and the existence of nongrowing perturbations has been highlighted for particular Atwood ratios (heavy to light), given implosion/explosion history and axial and azimuthal wave numbers. For a given gas combination, comparisons have been drawn between compressible numerical simulations of the RMI generated by self-similar converging shock waves and a plane-based model that considers the influence of the receding refracted waves and incorporates the asymptotic growth rate model developed in the first part of the paper in the case of a reflected shock. In addition, an extensive parametric study has been pursued. Results suggest that for small initial perturbations, the late-time decay of the dimensionless volume growth rate of the perturbed layer is nearly constant as the convergence ratio changes, and somehow independent of M_I and the type of geometry (the wave numbers and Atwood ratio having been fixed).

Studying the influence of the preshock Atwood ratio (e.g., heavy-to-light RMI) and different exploding configurations is left for possible future work, with the goal to compare the distinctive evolution of spikes and bubbles, as well as the existence of nongrowing modes. It would also be interesting to perform high-resolution three-dimensional cylindrical simulations initialized with small-amplitude axial and azimuthal modes, as suggested in Ref. 14 for the RTI. A step toward the comprehension of complex physical systems such as supernova would consist of considering multimode random perturbations of bigger amplitude and how the curved geometry affects the competition between different modes and spike/bubble structures.

ACKNOWLEDGMENTS

This work was supported by the Advanced Simulation and Computing (ASC) Program under Subcontract No. B341492 of DOE (Contract No. W-7405-ENG-48).

[1] R. D. Richtmyer, "Taylor instability in shock acceleration of compressible fluids," Commun. Pure Appl. Math. **13**, 297 (1960).
[2] E. E. Meshkov, "Instability of the interface of two gases accelerated by a shock wave," Fluid Dyn. **4**, 101 (1969).
[3] J. D. Lindl, *Inertial Confinement Fusion: The Quest for Ignition and Energy Gain Using Indirect Drive* (Springer, New York, 1998).
[4] B. Fryxell, E. Müller, and D. Arnett, "Instabilities and clumping in SN 1987A. I. Early evolution in two dimensions," Astrophys. J. **1991**, 619 (1984).
[5] S. Kumar, H. G. Hornung, and B. Sturtevant, "Growth of shocked gaseous interfaces in a conical geometry," Phys. Fluids **15**, 3194 (2003).
[6] N. E. Lanier, C. W. Barnes, S. H. Batha, R. D. Day, G. R. Magelssen, J. M. Scott, A. M. Dunne, K. W. Parker, and S. D. Rothman, "Multimode seeded Richtmyer–Meshkov mixing in a convergent, compressible, miscible plasma system," Phys. Plasmas **10**, 1816 (2003).
[7] S. H. R. Hosseini and K. Takayama, "Experimental study of Richtmyer–Meshkov instability induced by cylindrical shock waves," Phys. Fluids **17**, 084101 (2005).
[8] K. O. Mikaelian, "Rayleigh–Taylor and Richtmyer–Meshkov instabilities and mixing in stratified cylindrical shells," Phys. Fluids **17**, 094105 (2005).
[9] P. E. Dimotakis and R. Samtaney, "Planar shock cylindrical focusing by a perfect-gas lens," Phys. Fluids **18**, 031705 (2006).
[10] Q. Zhang and M. J. Graham, "A numerical study of Richtmyer–Meshkov instability driven by cylindrical shocks," Phys. Fluids **10**, 974 (1998).
[11] K. O. Mikaelian, "Rayleigh–Taylor and Richtmyer–Meshkov instabilities and mixing in stratified spherical shells," Phys. Rev. A **42**, 3400 (1990).
[12] J. G. Wouchuk, "Growth rate of the linear Richtmyer–Meshkov instability when a shock is reflected," Phys. Rev. E **63**, 056303 (2001).
[13] M. Lombardini and D. I. Pullin, "Startup process in the Richtmyer–Meshkov instability," Phys. Fluids **21**, 044104 (2009).
[14] H. Yu and D. Livescu, "Rayleigh–Taylor instability in cylindrical geometry with compressible fluids," Phys. Fluids **20**, 104103 (2008).
[15] G. I. Taylor, "The instability of liquid surfaces when accelerated in a direction perpendicular to their planes," Proc. R. Soc. London, Ser. A **201**, 192 (1950).
[16] M. S. Plesset, "On the stability of fluid flows with spherical symmetry," J. Appl. Phys. **25**, 96 (1954).
[17] G. I. Bell, "Taylor instability on cylinders and spheres in small amplitude approximation," Los Alamos Scientific Laboratory Report No. LA-1321, 1951.
[18] Y. Yang, Q. Zhang, and D. H. Sharp, "Small amplitude theory of Richtmyer–Meshkov instability," Phys. Fluids **6**, 1856 (1994).
[19] R. Deiterding, "Construction and application of an AMR algorithm for distributed memory computers," in *Adaptive Mesh Refinement—Theory and Applications*, Lecture Notes in Computational Science and Engineering Vol. 41, edited by T. Plewa, T. Linde, and V. G. Weirs (Springer, New York, 2005), pp. 361–372.
[20] M. J. Berger and J. Oliger, "Adaptive mesh refinement for hyperbolic partial-differential equations," J. Comput. Phys. **53**, 484 (1984).
[21] D. J. Hill and D. I. Pullin, "Hybrid tuned center-difference-WENO method for large eddy simulations in the presence of strong shocks," J. Comput. Phys. **194**, 435 (2004).
[22] C. Pantano, R. Deiterding, D. J. Hill, and D. I. Pullin, "A low numerical dissipation patch-based adaptive mesh refinement method for large-eddy

simulation of compressible flows," J. Comput. Phys. **221**, 63 (2007).
[23]R. F. Chisnell, "An analytic description of converging shock waves," J. Fluid Mech. **354**, 357 (1998).
[24]G. Guderley, "Starke Kugelige und zylindrische Verdichtungsstösse in der Nähe des Kugelmittelpunktes bzw der Zylinderachse," Luftfahrtforschung **19**, 302 (1942).
[25]W. Chester, "The quasi-cylindrical shock tube," Philos. Mag. **45**, 1293 (1954).
[26]R. F. Chisnell, "The normal motion of a shock wave through a nonuniform one-dimensional medium," Proc. R. Soc. London, Ser. A **232**, 350 (1955).
[27]G. B. Whitham, "On the propagation of shock waves through regions of non-uniform area or flow," J. Fluid Mech. **4**, 337 (1958).
[28]G. B. Whitham, *Linear and Nonlinear Waves* (Wiley-Interscience, New York, 1974), Sec. 8.1.
[29]P. Hafner, "Strong convergent shock waves near the center of convergence: A power series solution," SIAM J. Appl. Math. **48**, 1244 (1988).
[30]C. Bond, D. J. Hill, D. I. Meiron, and P. E. Dimotakis, "Shock structure in a planar convergent geometry with experiment and simulation," J. Fluid Mech. (in press).
[31]M. Lombardini, "Richtmyer–Meshkov instability in converging geometries," Ph.D. thesis, California Institute of Technology, 2008.
[32]S. T. Weir, E. A. Chandler, and B. T. Goodwin, "Rayleigh-Taylor instability experiments examining feedthrough growth in an incompressible geometry," Phys. Rev. Lett. **80**, 3763 (1998).